Recent progress in filtered Rayleigh scattering: Towards the simultaneous acquisition of pressure, temperature and three-component velocity fields

Ulrich Doll[1,*], Eike Burow[2], Guido Stockhausen[2], Christian Willert[2]
1: Laboratory of Thermal Processes and Combustion, Paul Scherrer Institute (PSI), Switzerland
2: Engine Measurement Systems, Institute of Propulsion Technology, German Aerospace Center (DLR), Germany
* Correspondent author: ulrich.doll@psi.ch

Keywords: Rayleigh scattering, molecular filter, Rayleigh lineshape, background correction, simultaneous measurement, temperature, pressure, velocimetry

ABSTRACT

The filtered Rayleigh scattering technique extended by the method of frequency scanning offers a viable option to efficiently characterize the aero-thermal properties of technical flows. The first part of the study is concerned with the identification and treatment of detrimental effects towards the methods uncertainty budget. Presented background correction as well as a novel approach with regard to the Rayleigh scattering's spectral distribution yields measurement accuracies for pressure, temperature and flow velocity below 15 hPa, 2.5 K and 2.7 m/s respectively. Based on an observation of the plane of interest from multiple views, an FRS velocimeter is brought into use, which is capable to simultaneously acquire pressure, temperature as well as three-component velocity maps.

1. Introduction

Originally developed for flow visualization in high-speed flows (Miles & Lempert, 1990; Miles et al, 1991), the filtered Rayleigh scattering technique (FRS), due to its potential to be used as planar temperature measurement method, was gradually adopted by several groups to acquire temperature fields in atmospheric laboratory flames (Elliott et al, 1997; Kearney et al, 2005; Most & Leipertz, 2001). As the technique utilizes molecular absorption to filter strong unwanted laser scattering from walls or windows, FRS appears to be perfectly suited to characterize internal flows. Nevertheless, the technique never matured beyond laboratory scale, which was mainly due an insufficient suppression of laser stray light caused by deficient spectral purity of the used laser light sources (Forkey, 1996; Kearney et al, 2005; Patton & Sutton, 2013).

In recent years the technique was adopted by DLR Cologne, where the focus was put towards turbomachinery applications. In aiming on time-averaged rather than instantaneous measurements, the system was implemented based on a continuous wave laser with excellent spectral characteristics. As a result, laser scattering from surfaces, which is omnipresent when

preforming measurements inside narrow flow channels, could be attenuated effectively. Adopting the so called frequency scanning method (FSM-FRS) introduced in Forkey (1996), the system has the capability to acquire time-averaged pressure, temperature and velocity maps simultaneously (Doll et al, 2014b). In addition, in order to minimize requirements regarding optical accessibility to the experiment, a probe-based implementation of the system was designed and realized, making use of fiber technology for high power laser light transfer as well as imaging. Several applications in non-reacting (Doll et al, 2015; Doll et al, 2014b) as well as high pressure combustion environments (Doll et al, 2012; Doll et al, 2017a; Schroll et al, 2017) have been realized utilizing the system.

After a short introduction to the theoretical foundations of the method, the first part of this contribution will summarize recent efforts to increase accuracies of FSM-FRS measurement results. In applying a background correction method as well as in utilizing a calibrated analytical formulation in order to model the Rayleigh scattering's spectral lineshape, deviations between FRS pressure, temperature and velocity results and a turbulent jet flow experiment are significantly reduced (Doll et al, 2016). In addition, a robust alternative mathematical model to interpret acquired FRS intensities is proposed, which confronts the issue of possible changes in the optical path between a reference experiment and the actual measurements under operating conditions (Doll et al, 2016). These methods are then applied in the evaluation of FRS data gathered in the near- as well as the far-field of a turbulent jet flow. In utilizing a multiple-branch image fiber bundle and thus observing the plane of interest from three directions, apart from pressure and temperature fields, three-component velocity distributions are reconstructed from these datasets (Doll et al, 2017b).

2. FSM-FRS theory and modeling

The filtered Rayleigh scattering technique makes use of the fact, that laser Rayleigh scattering from gas molecules is spectrally broadened due to the (mainly thermal) molecular motion, while intense laser light scattering from large particles (Mie scattering) or off surfaces has similar spectral characteristics as the incident radiation. The underlying principle of the FRS method is illustrated in Fig. 1, left. In tuning the laser's output frequency into the minimum of a molecular absorption line, the narrow-bandwidth portions of the scattering spectrum are strongly attenuated by the molecular filter, while shares of the Rayleigh scattering pass through and form the FRS signal (shaded areas in Fig. 1, left), which, in assuming the ideal gas law, holds

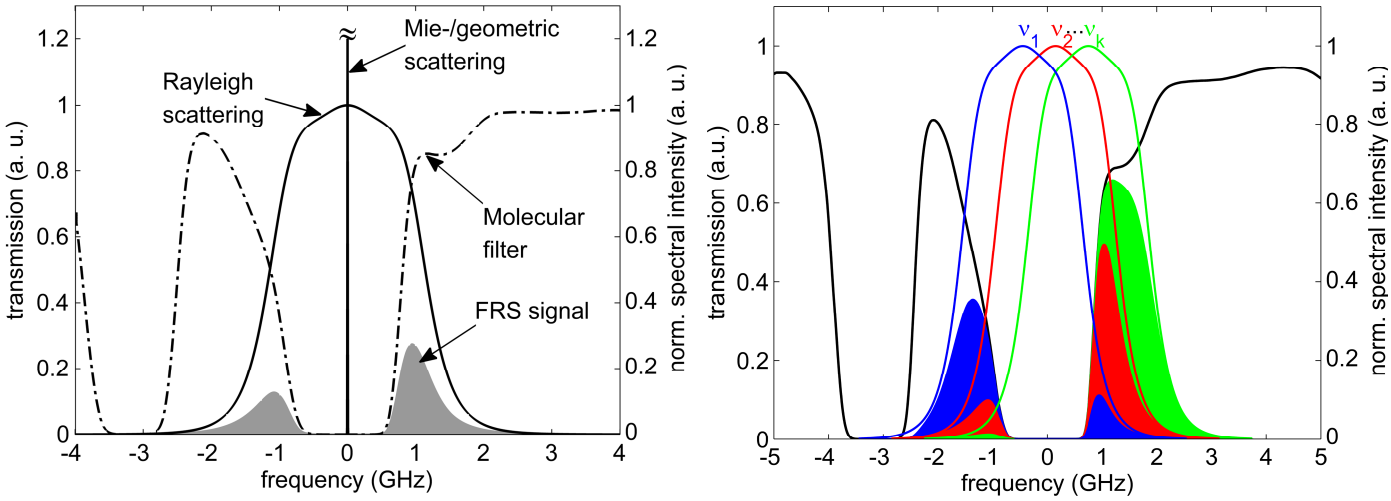

Fig. 1 (Left) Principle of FRS: Narrow-bandwidth laser light scattering from surfaces or large particles (Mie) is strongly attenuated, while portions of Rayleigh scattering pass through the filter. (Right) Frequency scanning method: tuning the laser's output frequency along the molecular filter's absorption line in discrete steps results in intensity spectra for each camera pixel.

information on pressure, temperature and flow velocity inside the observed volume element (Miles et al, 2001).

In FRS, image acquisition typically relies on CCD/CMOS[1] camera technology to capture light scattered from the planar region of interest. These devices are not sensitive to the spectral distribution of the FRS signal but rather detect a single intensity value per sensor element (integral of the shaded areas in Fig. 1, left). As this is not sufficient to simultaneously retrieve the information on pressure, temperature and velocity from the measured signal, the FRS technique is extended by a frequency scanning method. The idea of the method is depicted in Fig. 1, right: in scanning the laser's output frequency in discrete steps along the molecular filter's transmission curve and in acquiring images at the set frequencies, intensity spectra are generated at each sensor element. From these intensity spectra, time-averaged pressure, temperature and velocity maps can then be deduced.

The overall detected signal intensity at each sensor element ij at frequency step k can be written as (Doll et al, 2014b; 2017b; Forkey, 1996)

[1]charge-coupled device/complementary metal-oxide semiconductor

$$S_{ijkl}(\nu_{0,k}, p_{ij}, T_{ij}, \Delta\nu_{ijl}, \Theta_{ijl}) = R_{ijl} I_0 \left(n_{ij} \int_{-\infty}^{\infty} r_{ijl}(\nu - \nu_{0,k}, p_{ij}, T_{ij}, \Delta\nu_{ijl}, \Theta_{ijl})\, \tau(\nu)\, d\nu + C_{ijkl} \right). \quad (1)$$

The incident laser intensity is denoted by I_0, R is the optical setup's efficiency. The first expression in parentheses represents the FRS intensity, which corresponds to the convolution between the Rayleigh scattering's spectral lineshape r and the molecular filter's transmission curve τ, multiplied by the number density n. The term incorporates the dependencies of the measured signal with regard to laser's output frequency ν_0, pressure p, temperature T as well as the Doppler frequency-shift (due to flow velocity) $\Delta\nu$. The scattering geometry is expressed through the scattering angle $\Theta = \arccos(\boldsymbol{o} \cdot \boldsymbol{l})$, which is the angle between observer direction $\boldsymbol{o}$ and laser light direction $\boldsymbol{l}$. The second term on the right hand side of Eq. (1) indicates background intensities, which are induced by multiple scattering events between the optical surfaces inside the detector arrangement (Doll et al, 2016). This laser induced background is explicitly frequency dependent as well as it is liable to spatial variations of the intensity distribution inside the laser light sheet. It amounts to values in-between 5 % to 10 % of the total intensity detected at each sensor element and has to be accounted for. Data acquisition is carried out at scanning frequencies around the two neighboring absorption features (-3 GHz and 0 GHz) visible in Fig. 1, right, which, by raising the number of scanning frequencies, is significantly lowering the uncertainty limit of all measured quantities (Doll et al, 2014b). Scanning frequencies at both absorption lines are limited to regions, where the molecular filter is optically thick so that contributions from Mie or geometric scattering can be neglected (Doll et al, 2014b). Finally, the subscript l is added to denote for a variation of observer position with respect to the multiple-branch image fiber bundle utilized in the FRS velocimetry experiments presented further below.

An issue frequently experienced when applying the FSM-FRS technique in the characterization of technical flows is a change of the optical efficiency parameter R between a reference measurement with pressure as well as temperature known and zero flow velocity and the actual measurement at operating conditions. A variation in R may be caused by either events altering the laser's optical path towards the plane of interest or by changes in the detection arrangement's optical properties. An example of the former is presented in Doll et al (2014a), where refractive index variations due to a temperature stratification between vortex core and outer vortex region leads to a substantial redistribution of laser intensity. The latter can be related to movements of the investigated object, e. g. caused by thermal expansion during heat-up (Doll et al, 2017a) or a degrading quality of optical accessibility. If respective changes of the setup's optical properties

reach a steady state at the pre-defined experimental conditions, a normalization procedure can be applied (Doll et al, 2014a; Doll et al, 2016): in dividing the total detected intensity of Eq. (1) by its ensemble average over all frequencies, the resulting expression

$$Q_{ijkl} = \frac{S_{ijkl}}{\langle S_{ijl} \rangle} = \frac{n_{ij} \int_{-\infty}^{\infty} r_{ijl}\left(\nu - \nu_{0,k}, p_{ij}, T_{ij}, \Delta\nu_{ijl}, \Theta_{ijl}\right) \tau(\nu)\, d\nu + C_{ijkl}}{n_{ij} \frac{1}{k} \sum_{1}^{k} \left[\int_{-\infty}^{\infty} r_{ijl}\left(\nu - \nu_{0,k}, p_{ij}, T_{ij}, \Delta\nu_{ijl}, \Theta_{ijl}\right) \tau(\nu)\, d\nu\right]_k + C_{ijkl}} \tag{2}$$

becomes independent of the optical efficiency R. While the normalization procedure solves the issue of varying optical efficiencies between reference run and measuring at operating conditions, a drawback of the method lies in a reduction of the FRS signal's sensitivity to pressure: as a large part of the signal's pressure response is founded on the number density, dividing the total detected intensity by its ensemble average significantly reduces the influence of n in the modified formulation, so that pressure sensitivity will only be generated through associated changes in the Rayleigh scattering's spectral lineshape.

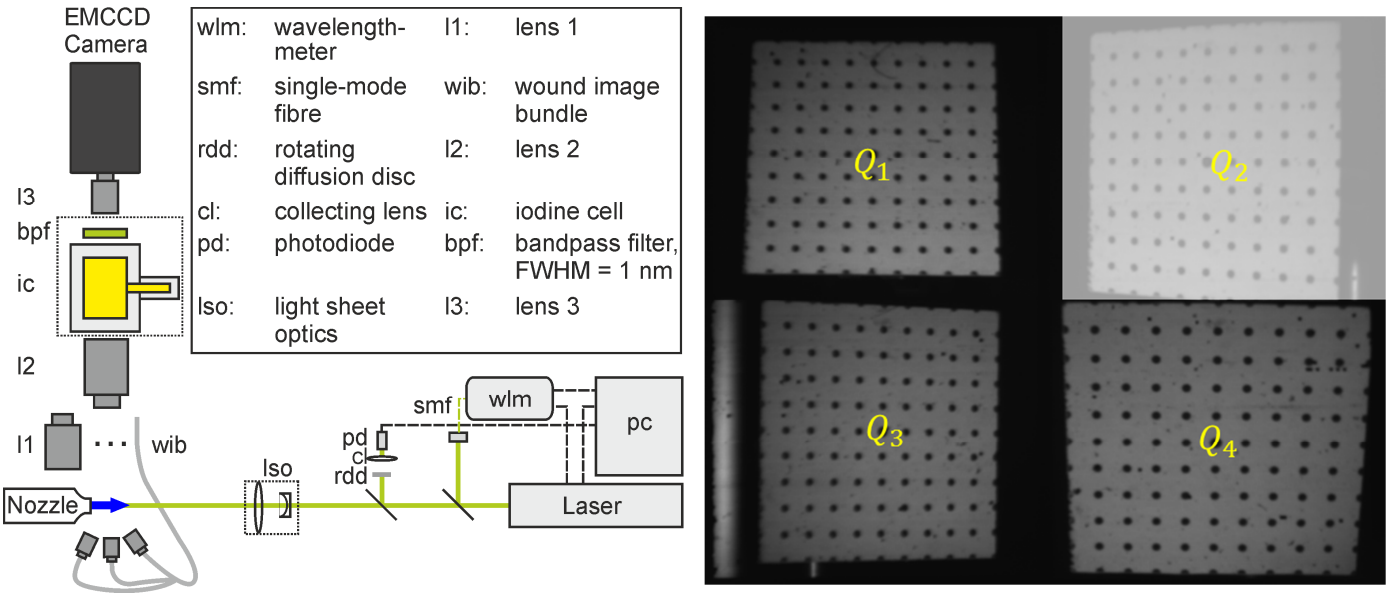

Fig. 2 (Left) Principle setup of FSM-FRS experiments. (Right) Calibration image obtained by utilizing a multiple-branch wound image bundle. Reprinted with permission from (Doll et al, 2016), IOP Publishing.

3. Experimental apparatus

A schematic of the FSM-FRS system's experimental arrangement is depicted in Fig. 2, left. The setup is based on a Coherent Verdi V5 continuous wave single-mode laser, emitting single-frequency laser light with a bandwidth <5 MHz and an adjustable output power of up to 5 W at 532 nm. In order to perform precise scanning of the laser's output frequency, the laser system features three options: a temperature controlled intra-cavity etalon can be used to coarsely adjust the frequency to reach the vicinity of a suitable molecular transition. In addition, by issuing control voltages onto two piezoelectric elements, the resonator length can be altered. Frequency monitoring and controlling is realized by two nested control loops based on a HighFinesse WSU 10 wavelength-meter, resulting in relative frequency deviations below 2 MHz as well as excellent long term frequency stability. To monitor the laser's output power, a small amount of laser light is deflected from the main beam by means of a thin glass plate and is directed onto a photodiode behind a rotating diffusion disc. The laser beam is then formed into a light sheet utilizing an optical scanner arrangement (Röhle & Willert, 2001) and finally illuminates the plane of interest.

Light scattered from the measurement plane is either gathered by a first camera lens or, alternatively, by a multiple-branch wound image bundle (Nobes et al, 2004). The latter is made up of four individual branches, which can each be equipped with standard C-mount lenses. Every branch has a light sensitive area of 6 x 5 mm^2, containing 600 x 500 single fiber elements. The multiple views are transferred through the individual branches and spliced at the fiber bundle's exit. The exit plane is then imaged onto the camera sensor. Fig. 2, right shows a calibration pattern, which is placed in the plane of interest and observed from different directions through the multiple-branch image fiber bundle. The image is divided into four equally sized quadrants, each representing one of the four camera views. Methods given in (Willert, 2006) are used to calibrate camera positions as well as to map the data onto a common Cartesian grid. As indicated by the transparent box, quadrant 2 is not used in the following experiments. After being collected by either a single camera lens or by the multiple-branch wound image bundle, light scattered from the plane of interest enters the detection unit's transfer optics, which is composed of two additional camera lenses in retro-arrangement, with the molecular iodine filter as well as a bandpass filter (Barr, FWHM 1 nm) placed in-between. The filtered radiation is finally accumulated by a Hamamatsu C9100-13 EM-CCD camera.

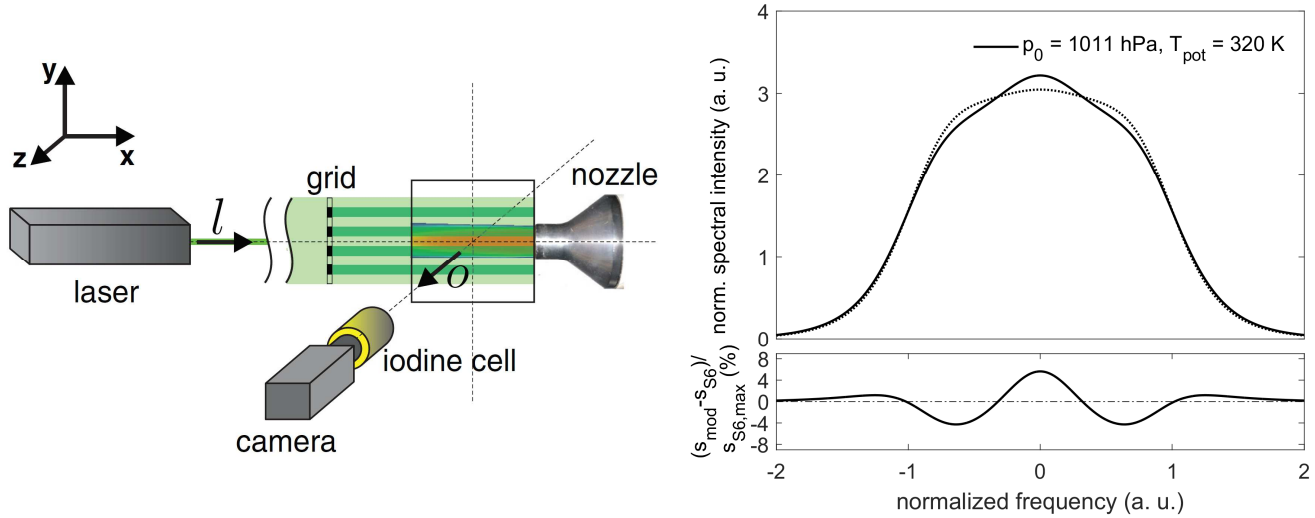

Fig. 3 (Left) Scattering geometry of near-field experiments with single front lens: the laser propagates along ***l***, scattered light is detected along ***o***. Images are acquired with homogeneous illumination as well as after introducing a metal grid into the beam path. Dark areas represent a portion of the laser induced background. (Right) Comparison between Rayleigh scattering lineshapes obtained with Tenti's S6 (dotted) model as well as calculated with the calibrated analytical lineshape model (solid). Relative differences between both models are shown below. Reprinted/adapted with permission from (Doll et al, 2016), IOP Publishing.

The investigated turbulent jet flow is emanating from a subcritical nozzle fed with compressed air. As flow conditions inside the jet's potential core can be assessed analytically, the experiment is used to verify proposed methods to reduce FSM-FRS measurement uncertainties. The nozzle has an exit diameter of 10 mm with a contraction area ratio of 36. The jet's potential core is imaged with the standard data acquisition setup utilizing a single camera lens. In the subsequent part of the experimental survey, the first camera lens is replaced by the wound image fiber-bundle. In two successive measurements, both the turbulent jet flow's potential core (near-field) as well as far-field topology are characterized in the modified optical arrangement. Latter experiments are carried out with a nozzle exit diameter of 20 mm, resulting in a reduced nozzle contraction area ratio of 9.

4. Results and discussion

4.1 Uncertainty reduction

In this section, deviations between analytically calculated aero-thermal flow conditions inside the turbulent jet flow's potential core and FSM-FRS measurement results are analyzed. As discussed previously, these deviations arise from an insufficient treatment of laser induced background intensities as well as a bias, which is introduced when using the standard Rayleigh scattering lineshape model by Tenti et al (1974). Methods to improve the accuracy of FSM-FRS measurement results are given below. A turbulent jet flow experiment is then used to test the effectiveness of the developed methodologies. Tab. 1 summarizes the five investigated operating points. The nozzle expands into air at ambient pressure p_0. Total pressure p_{tot} and temperature T_{tot} are measured within the nozzle plenum right before the expansion. These values are used to calculate the flow velocity v_{pot} as well as temperature T_{pot} inside the jet's potential core from isentropic relations. According to the scattering geometry depicted in Fig. 3, left, the jet flow expands against the laser propagation direction $\boldsymbol{l}$, with the camera oriented perpendicular to the measurement plane spanned by the light sheet along $\boldsymbol{o}$.

Tab. 1 Operating points of the jet flow experiment. Given uncertainties include hand-held pressure and temperature measurements as well as varying inlet pressures and temperatures. v_{pot} and T_{pot} as well as respective uncertainties are calculated from measured p_0, p_{tot} and T_{tot}. Adapted with permission from (Doll et al, 2016), IOP Publishing.

p_0 (hPa)	p_{tot} (hPa)	T_{tot} (K)	v_{pot} (m/s)	T_{pot} (K)
1004 ± 1	1021 ± 2	306 ± 2	-54 ± 3	304 ± 2
1004 ± 1	1041 ± 2	312 ± 2	-80 ± 2	308 ± 2
1005 ± 1	1071 ± 2	319 ± 2	-108 ± 2	313 ± 2
1011 ± 1	1100 ± 2	324 ± 2	-125 ± 1	316 ± 2
1011 ± 1	1124 ± 2	330 ± 2	-140 ± 1	321 ± 2

Background intensities produced inside the detector arrangement by laser scattering from optical surfaces are denoted by the parameter C of Eq. ((1)). In the standard data evaluation procedure, a constant value of C for all scanning frequencies is determined. Resulting deviations between measured/calculated pressure, temperature and flow velocity inside the jet's potential core and FSM-FRS measurement results obtained by using the original (Eq. (1)) as well as the

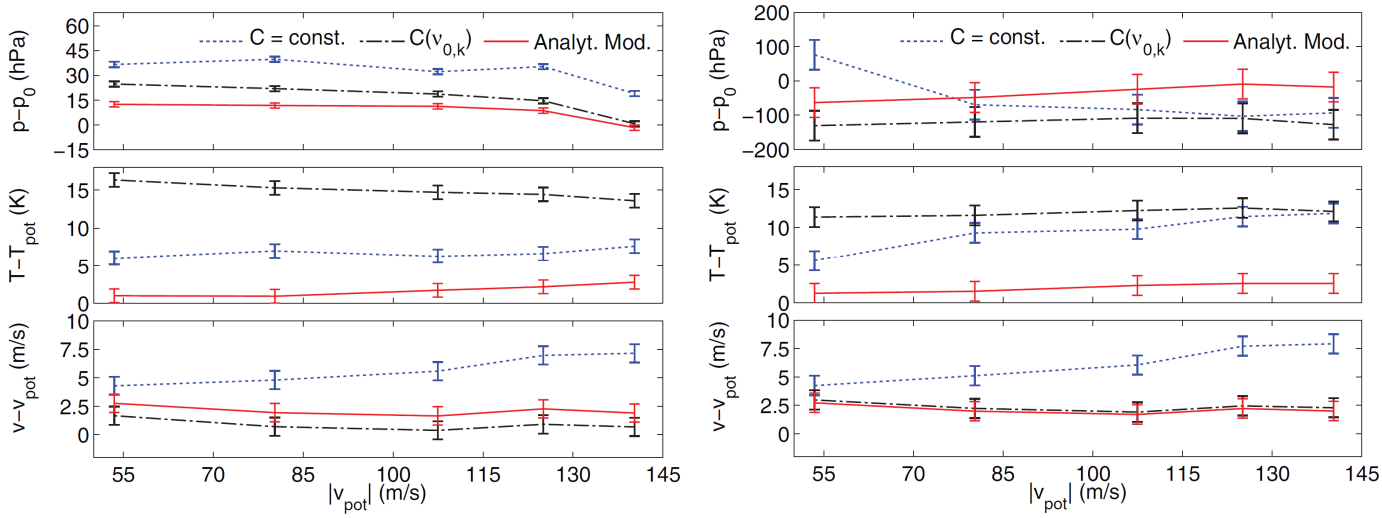

Fig. 4 Deviations between measured/calculated p_0, T_{pot}, v_{pot} and FSM-FRS results, spatially averaged over the jet's core region, assuming constant background (blue), employing the background correction (black) as well as the calibrated analytical lineshape model in addition (red) for original (Eq. ((1), left) and modified (Eq. ((2), right) model equation. Due to the normalization procedure, the modified model equation's pressure uncertainties exceed the original model equations by an order of magnitude. Adapted with permission from (Doll et al, 2016), IOP Publishing.

modified model equation (Eq. ((2)) are depicted in Fig. 4. Differences between reference temperatures and velocities are on similar level for both model equations, ranging from 5 K to 10 K and 4 m/s to 8 m/s, respectively. For pressure, values lie in-between 30 hPa to 40 hPa for the original formulation and -100 hPa to 100 hPa for the modified model equation. The significantly higher values in the latter case are caused by the already mentioned reduced pressure sensitivity caused by the normalization procedure.

To confront the frequency dependency of the laser induced background C, a correction method introduced in Schodl et al (2006) offers a viable option. The basic idea of the method is indicated in Fig. 3, left. First, an image at a certain scanning frequency and undisturbed homogeneous laser illumination is taken. By introducing a metal grid into the beam path, a regular pattern of dark and bright zones emerges, which is then captured in a second frame. Background intensities, which belong to the bright areas of the pattern, can now be extracted from the dark zones. Interpolating between these zones provides the background of the bar pattern image C_1. In a second step, an inverse bar pattern image is generated by subtracting the original frame from the image acquired with homogeneous illumination. Another interpolation between the

intensities of the dark zones of the inverse bar pattern image yields the second portion of the laser induced background C_2. Finally, in summing both shares, the background of the undisturbed image $C = C_1 + C_2$ is obtained.

The background correction's impact on FSM-FRS measurement accuracies is summarized in Fig. 4. Concerning velocities, the method leads to a reduction of deviations below 3 m/s for both original Eq. ((1) and modified Eq. ((2). Pressure differences are reduced for the original model equation, while exhibiting an elevated absolute level in case of the modified formulation. Temperature differences between reference values and FSM-FRS results increase for both model equations, however, in case of the original formulation by an significantly larger amount.

As after correcting for laser induced background the remaining signal portions should only contain FRS intensities, it is reasonable to associate the still persisting differences between FSM-FRS measurement results and reference experiment to an erroneous modelling of the Rayleigh scattering's spectral lineshape. Despite the standard model introduced by Tenti et al (1974) is well-established in FRS related literature, certain flaws of the model have been identified, e. g. the missing inclusion of inelastic scattering portions (Young & Kattawar, 1983; Zheng, 2007) or the dependency of the model on certain gas specific transport properties, including the so-called bulk (volume) viscosity, which, despite recent progress (Gu et al, 2013), is still controversial and defined for few thermodynamic conditions/gas species only (Meador et al, 1996; Pan et al, 2004). In order to reduce the detrimental impact of the lineshape modelling on FSM-FRS measurement accuracies, an analytical model is formulated in Doll et al (2016), which, after calibrating it based on experimental data, is covering the relevant thermodynamic range of the jet experiment. A comparison of two sample spectra calculated with S6 as well as calibrated analytical lineshape model is depicted in Fig. 3, right. The peak of the calibrated spectrum is more pronounced compared to the S6 model, while the influence or the Brillouin sidebands is less distinct. Deviations between both spectra amount of up to 5.7 % of the S6 model's peak value, which is significantly higher than differences of up to 2 % found in Gu et al (2013) and may point to an instrument function still not included in the FSM-FRS data evaluation scheme.

The impact of the calibrated analytical formulation on FSM-FRS measurement accuracies is inferred by utilizing both lineshape model as well as background correction in the data evaluation procedure. There is little effect on velocity accuracies related to the modified lineshape, which is in concurrence with the fact, that flow velocity is just shifting the Rayleigh scattering's spectral distribution in frequency space, but does not alter its spectral shape. With

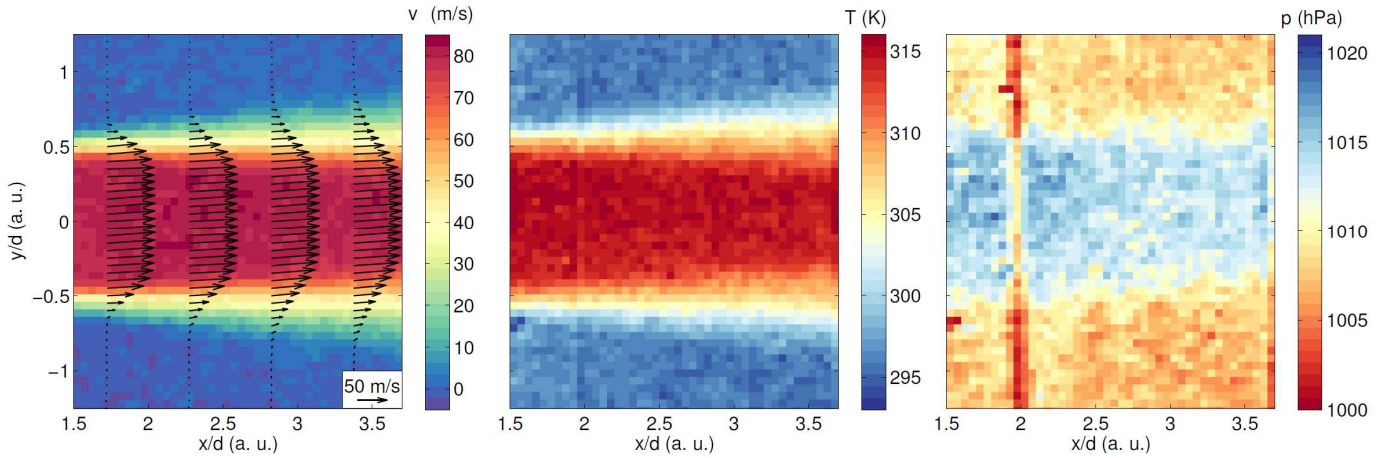

Fig. 5 Near-field results: main velocity component (horizontal, left), temperature (middle), and pressure fields (right). Velocity vectors indicate horizontal and vertical velocity components. Reprinted with permission from (Doll et al, 2017b), OSA Publishing.

regard to pressure as well as temperature however, differences between FSM-FRS measurement results and reference experiment are substantially reduced.

4.2 FRS velocimetry

Laser-optical three-component (3C) velocimetry methods such as stereoscopic particle image velocimetry (sPIV) and to a lesser extend Doppler global velocimetry (DGV) are well-established and widely used. However, both methods infer their measured signal by adding seeding particles to the flow, which have to be carefully chosen in order to follow the actual flow as well as to withstand potentially harsh flow conditions (Raffel et al, 2013). In addition, seed particles tend to form deposits on windows, which, due to the degrading quality of optical access to the experiment, in turn leads to reduced testing periods. In this section an FRS velocimeter is presented, which, in addition to time-averaged 3C velocity fields, is capable to deliver pressure as well as temperature distributions with single-pixel resolution. As the FRS technique relies on molecular scattering only, no tracer particles have to be added to the flow, making the FRS technique a viable alternative to established measuring approaches under certain flow and environmental conditions.

Velocity measurements by FRS are expressed through the optical Doppler frequency-shift

$$\Delta\nu = \frac{\nu_0}{c}(\boldsymbol{o} - \boldsymbol{l}) \cdot \boldsymbol{v}\,. \tag{3}$$

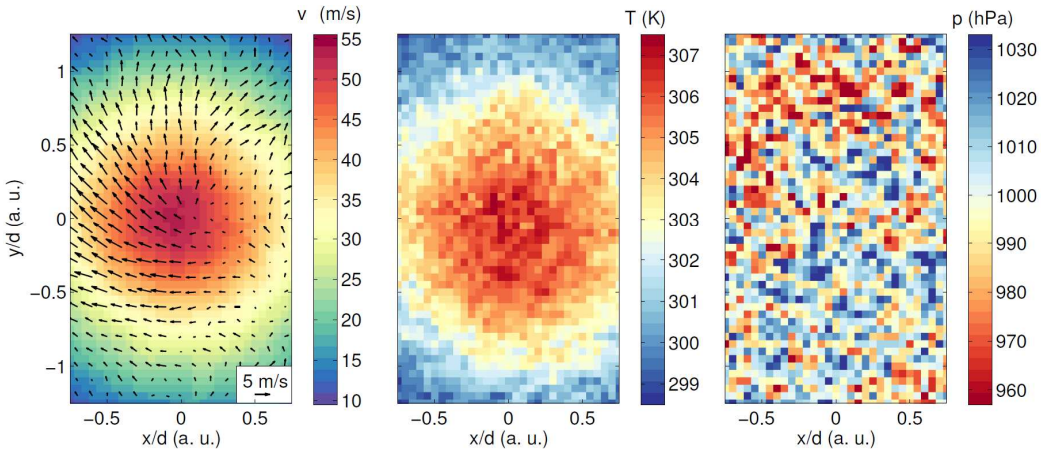

Fig. 6 Far-field results: main velocity component (out-of-plane, left), temperature (middle), and pressure fields (right). Velocity vectors indicate horizontal and vertical velocity components. Reprinted with permission from (Doll et al, 2017b), OSA Publishing.

Hence, either light sheet orientation or observer position have to be varied to reconstruct 3C velocities from an FRS dataset (Meyers & Komine, 1991). The latter is realized in this contribution. By means of the multiple-branch wound image bundle introduced in Sec. 3, the plane of interest is observed from three directions. While temperature and pressure are the same for all views, the varying scattering geometry leads to differing Doppler frequency-shifts, from which the 3C velocity field can then be reconstructed. As proof of concept, the near-field as well as the far-field flow of a turbulent jet flow experiment is investigated by FRS velocimetry.

Fig. 5 shows simultaneously acquired time-averaged pressure, temperature and 3C velocity maps of the turbulent jets near-field. Velocity and temperature map exhibit a typical near-field distribution: values in the jet's potential core are constant, while strong gradients in the growing top and bottom shear layers emerge. Outside the jet, almost ambient conditions are reached. The weak upward orientation of depicted velocity vectors is associated with a slight misalignment of the jet axis with regard to the measurement plane. As the jet expands into ambient air, the pressure should be constant throughout the imaged area. However, a slightly increased pressure inside the potential core is in line with the findings of Sec. 4.1, where, after applying the calibrated analytical Rayleigh lineshape model, a deviation between reference and FSM-FRS pressure results of up to 15 hPa is still persistent. Finally, the artifact in the pressure map visible at $x/d = 2$ can be attributed to a contamination of the sheet optics between reference run and actual measurement.

The results of the far-field characterization are visualized in Fig. 6. As stability issues with regard to the optical setup were identified between reference run and the actual measurement at operating conditions, the far-field data is evaluated based on the modified model Eq. (2). This finds its expression by the heightened spatial pressure variation of ±19 hPa compared to near-field results. Velocity and temperature, however, exhibit the typical Gaussian topology of a fully developed turbulent jet flow. The slight upward orientation of the vector field is again attributed to the misalignment between nozzle axis and light sheet.

5. Conclusion

The contribution summarizes recent efforts to provide methods to reduce uncertainties of FSM-FRS measurement results as well as to exploit the FSM-FRS methods capabilities to simultaneously provide time-averaged pressure, temperature and three-component velocity fields. A background correction methodology as well as a calibrated analytical formulation for the modelling of the Rayleigh scattering's spectral shape are introduced. Both methods are tested on a turbulent jet flow experiment, reducing pressure, temperature and velocity deviations to an analytically calculated reference solution below 15 hPa, 2.5 K and 2.7 m/s, respectively. The contribution is subsequently concerned with the realization of an FRS velocimeter. Based on a multiple-branch wound image bundle, the plane of interest is observed from multiple directions. The resulting variation of Doppler frequency-shifts for each camera view enables the reconstruction of a three-component velocity vector at each sensor pixel. Hence, FRS offers a viable alternative to existing (seeding based) velocimetry approaches, providing three-component velocity fields as well as temperature and pressure distributions simultaneously.

References

Doll, U., Beversdorff, M., Stockhausen, G., Willert, C., Morsbach, C., Schlüß, D. & Franke, M. (2015) The flow field inside a Ranque-Hilsch vortex tube part I: Experimental analysis using planar filtered Rayleigh scattering, *The ninth Symposium on Turbulence and Shear Flow Phenomena (TSFP-9)*.

Doll, U., Beversdorff, M., Stockhausen, G., Willert, C., Schlüß, D. & Morsbach, C. (2014a) Characterization of the flow field inside a Ranque-Hilsch vortex tube using filtered Rayleigh scattering, Laser-2-Focus velocimetry and numerical methods, *17th Int Symp on Applications of Laser Techniques to Fluid Mechanics*.

Doll, U., Burow, E., Stockhausen, G. & Willert, C. (2016) Methods to improve pressure, temperature and velocity accuracies of filtered Rayleigh scattering measurements in gaseous flows. *Measurement Science and Technology*, 27(12), 125204-125204.

Doll, U., Fischer, M., Stockhausen, G. & Willert, C. (2012) Frequency scanning filtered Rayleigh scattering in combustion experiments, *16th Int Symp on Applications of Laser Techniques to Fluid Mechanics*.

Doll, U., Stockhausen, G., Heinze, J., Meier, U., Hassa, C. & Bagchi, I. (2017a) Temperature Measurements at the Outlet of a Lean Burn Single-Sector Combustor by Laser Optical Methods. *Journal of Engineering for Gas Turbines and Power*, 139(2), 021507-021507.

Doll, U., Stockhausen, G. & Willert, C. (2014b) Endoscopic filtered Rayleigh scattering for the analysis of ducted gas flows. *Experiments in Fluids*, 55(3), 1-13.

Doll, U., Stockhausen, G. & Willert, C. (2017b) Pressure, temperature, and three-component velocity fields by filtered Rayleigh scattering velocimetry. *Opt. Lett.*, 42(19), 3773-3776.

Elliott, G., Glumac, N., Carter, C. & Nejad, A. (1997) Two-Dimensional Temperature Field Measurements Using a Molecular Filter Based Technique. *Combustion Science and Technology*, 125(1), 351-369.

Forkey, J. (1996) *Development and Demonstration of Filtered Rayleigh Scattering: a Laser Based Flow Diagnostic for Planar Measurement of Velocity, Temperature and Pressure*Princeton University.

Gu, Z., Witschas, B., van de Water, W. & Ubachs, W. (2013) Rayleigh-Brillouin scattering profiles of air at different temperatures and pressures. *Appl. Opt.*, 52(19), 4640-4651.

Kearney, S., Schefer, R., Beresh, S. & Grasser, T. (2005) Temperature imaging in nonpremixed flames by joint filtered Rayleigh and Raman scattering. *Appl. Opt.*, 44(9), 1548-1558.

Meador, W. E., Miner, G. A. & Townsend, L. W. (1996) Bulk viscosity as a relaxation parameter: Fact or fiction? *Physics of Fluids*, 8(1), 258-261.

Meyers, J. F. & Komine, H. (1991) Doppler global velocimetry-A new way to look at velocity, *Laser Anemometry-Advances and Applications 1991*.

Miles, R. & Lempert, W. (1990) Two-dimensional measurement of density, velocity, and temperature in turbulent high-speed air flows by UV Rayleigh scattering. *Applied Physics B: Lasers and Optics*, 51, 1-7.

Miles, R., Lempert, W. & Forkey, J. (1991) Instantaneous velocity fields and background suppression by filtered Rayleigh scattering, *29th AIAA Aerospace Sciences Meeting*. 1991.

Miles, R., Yalin, A., Tang, Z., Zaidi, S. & Forkey, J. (2001) Flow field imaging through sharp-edged atomic and molecular notch filters. *Measurement Science and Technology*, 12(4), 442-442.

Most, D. & Leipertz, A. (2001) Simultaneous Two-Dimensional Flow Velocity and Gas Temperature Measurements by use of a Combined Particle Image Velocimetry and Filtered Rayleigh Scattering Technique. *Appl. Opt.*, 40(30), 5379-5387.

Pan, X., Schneider, M. N. & Miles, R. B. (2004) Coherent Rayleigh-Brillouin scattering in polyatomic gases, *Quantum Electronics and Laser Science, 2003. QELS. Postconference Digest*.

Patton, R. & Sutton, J. (2013) Seed laser power effects on the spectral purity of Q-switched Nd:YAG lasers and the implications for filtered rayleigh scattering measurements. *Applied Physics B: Lasers and Optics*, 111(3), 457-468.

Raffel, M., Willert, C. E., Kompenhans, J. u. & others (2013) *Particle image velocimetry: a practical guide*Springer.

Röhle, I. & Willert, C. (2001) Extension of Doppler global velocimetry to periodic flows. *Measurement Science and Technology*, 12(4), 420-420.

Schodl, R., Stockhausen, G., Willert, C. & Klinner, J. (2006) Komplementär-Streifen-Verfahren für die Doppler Global Velocimetry (DGV), *14. GALA Fachtagung Lasermethoden in der Strömungsmesstechnik*.

Schroll, M., Doll, U., Stockhausen, G., Meier, U., Willert, C., Hassa, C. & Bagchi, I. (2017) Flow Field Characterization at the Outlet of a Lean Burn Single-Sector Combustor by Laser-Optical Methods. *Journal of Engineering for Gas Turbines and Power*, 139(1), 011503-011503.

Tenti, G., Boley, C. D. & Desai, R. C. (1974) On the Kinetic Model Description of Rayleigh-Brillouin Scattering from Molecular Gases. *Canadian Journal of Physics*, 52(4), 285-290.

Willert, C. (2006) Assessment of camera models for use in planar velocimetry calibration. *Experiments in Fluids*, 41(1), 135-143.

Young, A. T. & Kattawar, G. W. (1983) Rayleigh-scattering line profiles. *Appl. Opt.*, 22(23), 3668-3670.

Zheng, Q. (2007) Model for polarized and depolarized Rayleigh Brillouin scattering spectra in molecular gases. *Opt. Express*, 15(21), 14257-14265.